MOEM

Modern Electronic Materials 2023; 9(2): 45–56
DOI 10.3897/j.moem.9.2.109827

Research Article

Thermal and thermoelectric properties of metal-doped zinc oxide ceramics

Aliaksei V. Pashkevich[1,2], Alexander K. Fedotov[1], Eugen N. Poddenezhny[3], Liudmila A. Bliznyuk[4], Vladimir V. Khovaylo[5], Vera V. Fedotova[4], Andrei A. Kharchenko[1]

1 *Research Institute for Nuclear Problems of Belarusian State University, 11 Bobruiskaya Str., Minsk, 220006, Republic of Belarus*
2 *Belarusian State University, 4 Niezaliežnasci Ave., Minsk 220030, Republic of Belarus*
3 *Sukhoi State Technical University of Gomel, 48 Oktyabrya Ave., Gomel 246746, Republic of Belarus*
4 *Scientific-Practical Materials Research Centre of the National Academy of Sciences of Belarus, 19 P. Brovka Str., Minsk 220072, Republic of Belarus*
5 *National University of Science and Technology "MISIS", 4-1 Leninsky Ave., Moscow 119049, Russian Federation*

Corresponding author: Aliaksei V. Pashkevich (alexei.pashckevich@yandex.by)

Received 25 March 2023 ♦ **Accepted** 10 June 2023 ♦ **Published** 5 July 2023

Citation: Pashkevich AV, Fedotov AK, Poddenezhny EN, Bliznyuk LA, Khovaylo VV, Fedotova VV, Kharchanko AA (2023) Thermal and thermoelectric properties of metal-doped zinc oxide ceramics. *Modern Electronic Materials* 9(2): 45–56. https://doi.org/10.3897/j.moem.9.2.109827

Abstract

The thermal, electrical and thermoelectric properties of ZnO–Me_xO_y ceramics with $1 \le x, y \le 3$, where *Me* = Al, Co, Fe, Ni, Ti, have been studied. The specimens have been synthesized using the ceramic sintering technology from two or more oxides in an open atmosphere with annealing temperature and time variation. The structural and phase data on the ceramics have shown that post-synthesis addition of Me_xO_y doping powders to wurtzite-structured ZnO powder causes $Zn_x(Me)_yO_4$ spinel-like second phase precipitation and a 4-fold growth of ceramics porosity. Room temperature heat conductivity studies have testified to predominant lattice contribution. A decrease in the heat conductivity upon doping proves to be caused by phonon scattering intensification due to the following factors: size factor upon zinc ion substitution in the ZnO lattice (wurtzite) by Me_xO_y doping oxide metal ions; defect formation, i.e., point defects, grain boundaries (microstructure refinement); porosity growth (density decline); secondary phase particle nucleation ($Zn_x(Me)_yO_4$ spinel-like ones). The above listed factors entailed by zinc ion substitution for metal ions (Co, Al, Ti, Ni, Fe) increase the figure-of-merit *ZT* by four orders of magnitude (due to a decrease in the electrical resistivity and heat conductivity coupled with a moderate thermo-emf decline). The decrease in the electrical resistivity originates from a more homogeneous distribution of doping metal ions in the wurtzite lattice upon longer annealing which increases the number of donor centers.

Keywords

ceramics, zinc oxide, density, heat conductivity, phonon scattering, thermoelectric efficiency

1. Introduction

Zinc oxide possesses a unique combination of physical properties and can be produced by a wide variety of methods. This has made it the subject of close attention of researchers for many decades. ZnO based ceramics find increasingly wide application in gages and various electric transducers [1, 2], gas sensors [3], high-power electronics where heat removal is of great importance [4] and other domains. Investigations aimed at improving the

properties and broadening the applications of these materials are currently focused on the search for various combinations of doping elements, such as transition metals **(TM)**. Ceramics have a number of advantages over single crystals, polycrystalline ingots and thin films as well as other ZnO based materials requiring more expensive technologies. Ceramic technologies provide items of any shapes and sizes having various morphologies of structural inclusions (grains and phases). This provides for efficient control of the functionality of ceramics by varying the temperature, atmosphere and time of synthesis and post-synthesis heat treatment as well as doping element type added to initial powder mixtures [5–10]. However, to attain a composition with required combinations of properties one should identify correlations between the structure (phase and chemical composition), morphology (grain shape, porosity, size distribution, etc.), electrical and thermal properties of zinc oxide based composite ceramics and search for more resource-saving technologies [5–7, 11, 12].

In this work we studied the abovementioned relations favorable for ZnO based ceramic application as *n*-type conductivity thermoelectric materials that can be quite promising due to their high electron mobility, thermal stability and corrosion resistance as well as low health and environment hazard. However, the heat conductivity of undoped ZnO is so high that its dimensionless figure-of-merit *ZT* turns out to be far lower than required for industrial application. The figure-of-merit can be calculated using the following formula:

$$ZT = \frac{S^2 T}{(\kappa_l + \kappa_e)\rho}; \quad (1)$$

$$\kappa = \kappa_l + \kappa_e = \lambda C_p d_0, \quad (2)$$

where Z is the efficiency, T is the absolute temperature, S is the thermo-emf coefficient, ρ is the electrical resistivity, κ_l is the lattice heat conductivity coefficient, κ_e is the electron conductivity coefficient, λ is the temperature conductivity coefficient, C_p is the isobaric heat capacity and d_0 is the density of specimens.

Therefore thermoelectric applications require the heat conductivity (it consists of two contributions, i.e., the lattice one κ_l and the electron one κ_e) and electrical resistivity ρ of the material be greatly reduced without reducing S.

From this standpoint, doping is one of the key tools to tune the κ, S and ρ parameters for increasing the thermoelectric efficiency ZT in Eq. (1). Since the direct measurement of the heat conductivity coefficient κ is quite a labor-consuming task, it is often assessed with a simpler technique, i.e., laser flash temperature conductivity coefficient measurement.

Literary sources contain a large number of ZnO based material doping options for microstructure controlling aimed at matching the thermoelectric and transport properties. There are data [13–19] on the effect of doping elements such as Al, Bi, Co, Fe, Ni, Ga, Mn, Sb, Sn and pairwise combinations thereof on the thermoelectric and transport properties of these materials. The cited works contain helpful information on the relation between the structure and various properties obtained as a result of doping. However, there is no systematic study of the correlation between the thermoelectric and thermal properties, as well as the microstructure, phase composition and morphology (porosity, grain size) in films and ceramics [20, 21]. Multiple experimental and theoretical works showed that there are two efficient methods to reduce the heat conductivity: formation of substitution alloys and nanostructuring (e.g. by reducing grain sizes, introducing pores and nanosized phase inclusions) [22].

Presented below are experimental data on ceramics formed from zinc oxide and metal oxides such as ZnO–Me_xO_y with $1 \le x, y \le 3$, where Me = Al, Co, Fe, Ni, Ti. The aim of the experiments was to study the effect of ceramic composition on the matching of thermoelectric, thermal and electrical properties.

2. Specimens and methods

ZnO based specimens were synthesized using the ceramic sintering technology from two or more oxides in an open atmosphere. The initial components for the charge were ZnO and Me_xO_y powder mixtures of the following compositions: 10 wt.% CoO, 3–5 wt.% Al_2O_3, 10 wt.% TiO_2. The charge composition for the test ceramic specimens was designed based on the formula $(ZnO)_{100-z}(Me_xO_y)_z$, where z = 3÷10 wt.% is the metal oxide powder weight percentage in the test specimens. Most of the specimens were in the form of compacted tablets fabricated by single-step calcination, while the $(ZnO)_{90}(CoO)_{10}$-2 specimens were sintered in two step sintering process after compaction as described earlier [23, 24]. Details on the

Table 1. Test specimen composition and synthesis mode notations

#	Specimen	Preliminary/final sintering temperature, K	Preliminary/final sintering time, h
1	ZnO	1373	2
2	$(ZnO)_{90}(CoO)_{10}$-2*	1173/1473	2/2
3	$(ZnO)_{97}(Al_2O_3)_3$	1473	3
4	$(ZnO)_{95}(Al_2O_3)_5$	1473	3
5	$(ZnO)_{97}(Al_2O_3)_3$	1473	3
6	$(ZnO)_{96.5}(Al_2O_3)_3(NiO)_{0.5}$	1473	3
7	$(ZnO)_{96.5}(Al_2O_3)_3(Fe_2O_3)_{0.5}$	1473	3
8	$(ZnO)_{96.5}(Al_2O_3)_3(Fe_3O_4–SiO_2)_{0.5}$	1473	3
9	$(ZnO)_{90}(TiO_2)_{10}$	1473	3

* Digit "2" at the end of specimen notation means two-stage annealing.

compositions and annealing modes for the specimens are summarized in Table 1. Specimens 3 and 5 differ in the origin of the raw ZnO powders.

The matrix phase structure and the phase composition of the synthesized specimens were studied using X-ray diffraction **(XRD)** at room temperature on a DRON-3 M diffractometer with CuK_α radiation. The data were processed with the Math!(3.14 Build 238) and FullProf software by XRD pattern deconvolution into integral intensities. The following ceramic phase identification crystallographic database cards were used:

– ZnO #96-900-4179;
– $ZnFe_2O_4$ #96-900-5108;
– $ZnCo_2O_4$ #96-591-0137 (or Co_3O_4 #96-900-5888);
– Zn_2TiO_4 #96-900-1693;
– $ZnAl_2O_4$ #96-900-6202.

The FullProf software uses Rietveld (full-profile) analysis designed for neutron and X-ray diffraction studies [25]. The structural morphology and the chemical composition of the synthesized ceramics were studied under TescanVega 3LMU and LEO 1455 VP scanning electron microscopes (SEM) with EDX attachments for determining component concentrations in the composites. Details of operation and results provided by the method were described earlier [26].

For room temperature measurements of the electrical resistivity, thermo-emf coefficient S and density, the synthesized ceramic tablets were cut into rectangular specimens 2–3 mm in width and 7–10 mm in length. Indium was applied to the butt-ends of the specimens with an ultrasonic soldering for more homogeneous current distribution by the specimen and thermal resistivity reduction. The Seebeck coefficient S and the electrical resistivity were measured at room temperature using measuring system with a moving copper-tip as gradient heater, Agilent 34410A and Agilent 34411A multimeters. The butt-end temperature of the specimen placed in the metering system was monitored with RT-100M platinum thermometers. The heat conductivity λ was measured for 8.8×1.5 mm^2 ceramic specimens in the T = 300÷573 K range by the laser flash method with LFA 467 (Netzch, Germany) and TC-1000 (Ulvac-Riko, Japan) analyzers.

3. Structure and phase composition of composite ceramics

The XRD and EDX data (Fig. 1, Table 2) suggest that CoO, Al_2O_3 and TiO_2 additions to ZnO cause the formation of not only the ZnO wurtzite tetragonal phase (Specimen 1, see Fig. 1 *a* and Fig. 1, *f*), but also the second $Zn_x(Me)_yO_4$ cubic phases ($ZnCo_2O_4$, $ZnAl_2O_4$, Zn_2TiO_4 and $ZnFe_2O_4$ for Co, Al, Ti and Fe doping, respectively), where x = 1÷2 and y = 1÷2 (Specimens 2–9, see Fig. 1 *a* and Fig. 1 *b–e*) [27]. The X-ray peaks for the two-stage annealed specimen containing 10 wt.% CoO (Speci-

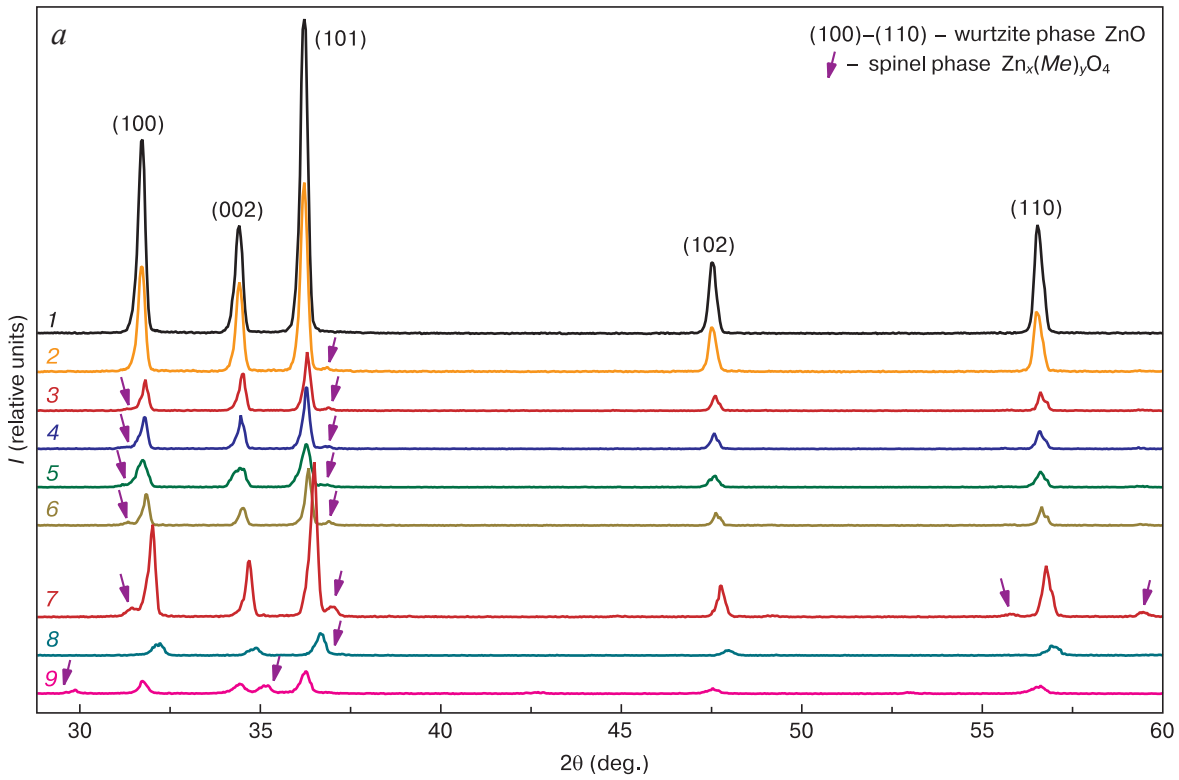

Figure 1. (*a*) X-ray patterns for ZnO based ceramic, (*b*) EDX data for element distributions (*c–f*) for $(ZnO)_{96.5}(Al_2O_3)_3(Fe_3O_4–SiO_2)_{0.5}$: (*1*) ZnO; (*2*) $(ZnO)_{90}(CoO)_{10}$-2; (*3*) $ZnO)_{97}(Al_2O_3)_3$; (*4*) $ZnO)_{95}(Al_2O_3)_5$; (*5*) $ZnO)_{97}(Al_2O_3)_3$; (*6*) $(ZnO)_{96.5}(Al_2O_3)_3(NiO)_{0.5}$; (*7*) $(ZnO)_{96.5}(Al_2O_3)_3(Fe_2O_3)_{0.5}$; (*8*) $ZnO)_{96.5}(Al_2O_3)_3(Fe_3O_4–SiO_2)_{0.5}$; (*9*) $(ZnO)_{90}(TiO_2)_{10}$

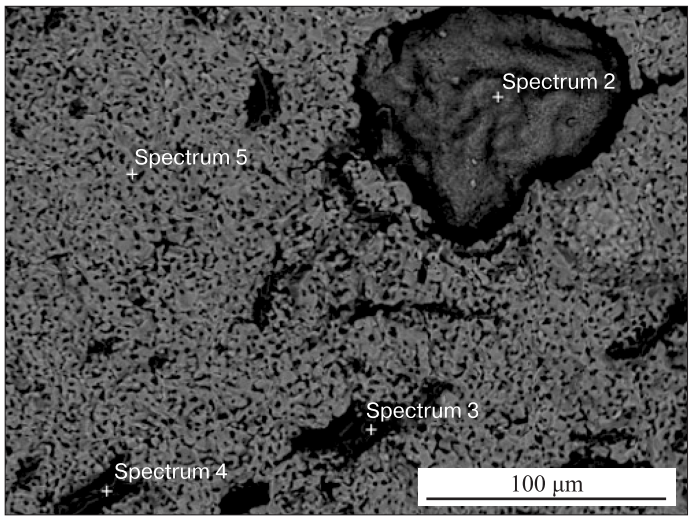

b

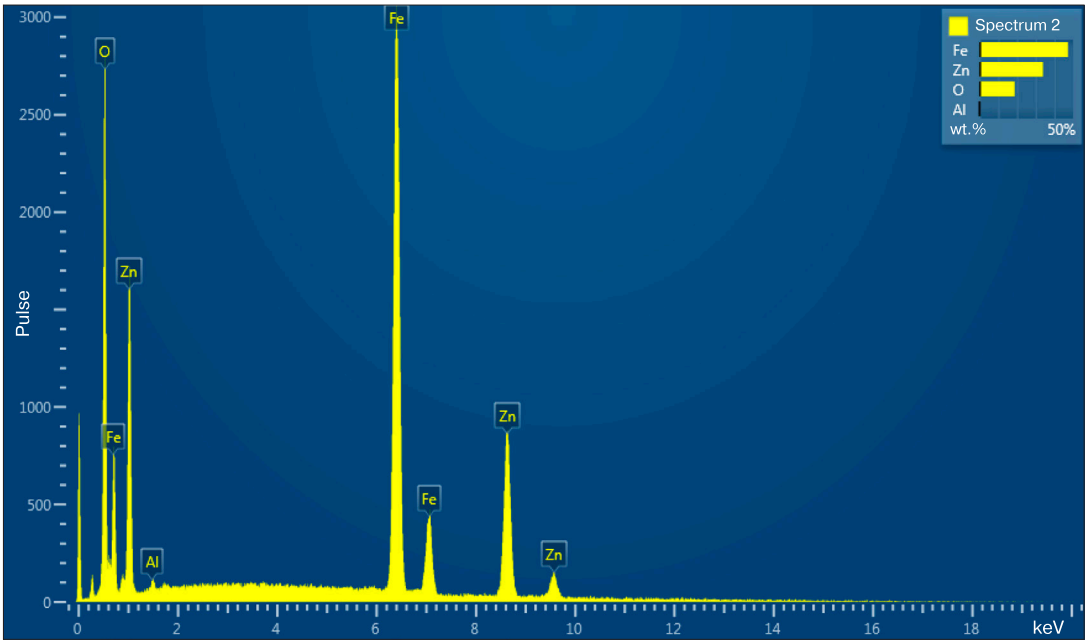

c

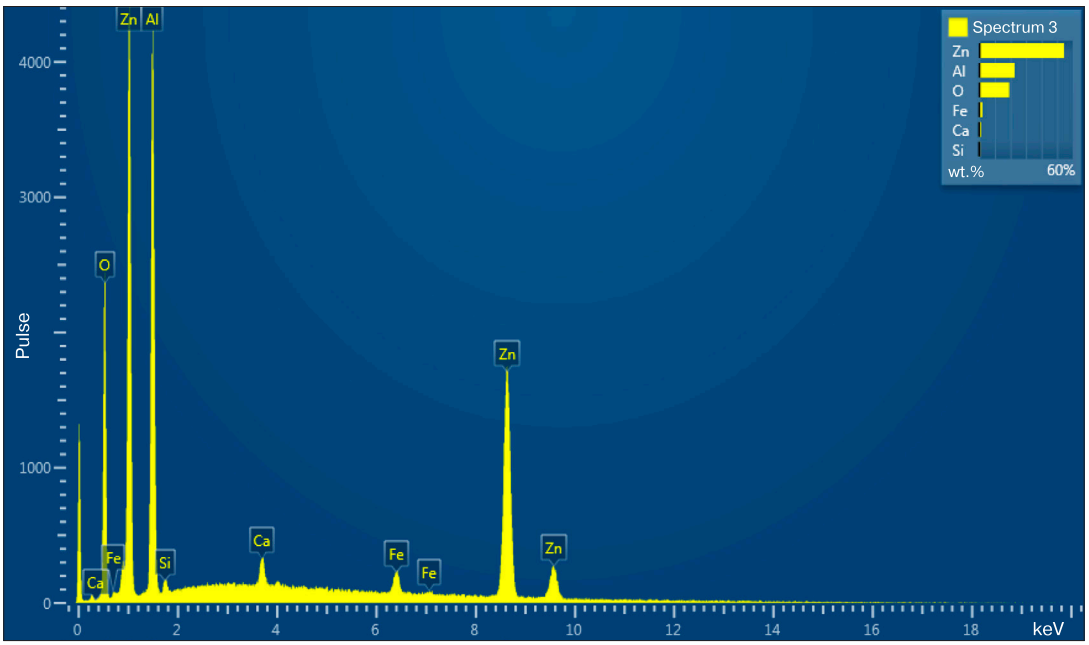

d

Figure 1. (*b–d*), continuation

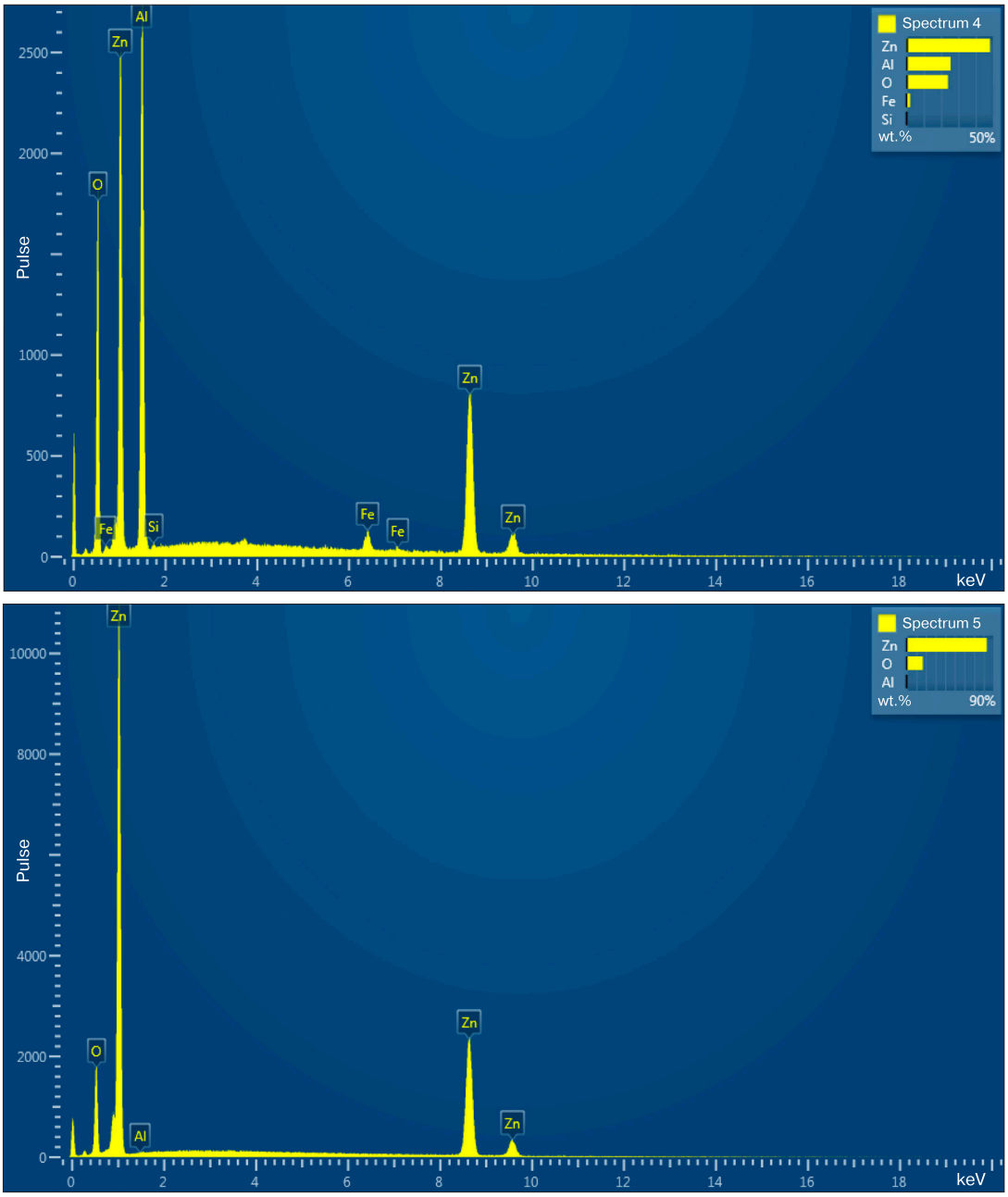

Figure 1. (*e–f*), ending

men 2, see Fig. 1 *a*) suggest a relatively low content of the $ZnCo_2O_4$ (or Co_3O_4) phase provided that most Co ions have substituted Zn ones in the ZnO lattice [22].

The X-ray patterns of the specimens shown in Fig. 1 *a* suggest that additions of 3–5 wt.% Al_2O_3 (Specimens 3–8) and 10 wt.% TiO_2 (Specimen 9) to zinc oxide ceramics cause Al and Ti incorporation into the ZnO wurtzite phase lattice (Fig. 1 *b, f*) and the formation of the $Zn_x(Me)_yO_4 : ZnAl_2O_4$ cubic phases for the Al doped specimens [28] (Specimens 3–8, see Fig. 1 *d*, *e* and Fig. 2 *h*) and the Zn_2TiO_4 cubic phases for the Ti doped specimen (Specimen 9) [18]. For Specimens 6–8, addition of 0.5 wt.% NiO [29], Fe_2O_3 and Fe_3O_4–SiO_2 also causes the formation of $Zn_x(Me)_yO_4$ phases in small quantities, e.g., $ZnFe_2O_4$ [14, 20, 21] for the $(ZnO)_{96.5}(Al_2O_3)_3(Fe_3O_4–SiO_2)_{0,5}$ specimen (Specimen 8) which is shown in Fig. 1 *c*.

The XRD-determined lattice parameters allowed evaluating the X-ray densities of the material d_1, d_2 and d_3 (in kg/m^3) using the following relationships:

– for the ZnO phase:

$$d_1 = \frac{N_1 A_1}{V_1} = N_1 A_1 \Big/ \frac{6a^2\sqrt{3}}{4} C = \frac{2N_1 A_1}{3\sqrt{3}a^2 c}; \quad (3)$$

– for the $Zn_x(Me)_yO_4$ phase:

$$d_2 = \frac{N_2 A_2}{V_2} = \frac{N_2 A_2}{b^3}; \quad (4)$$

Table 2. Calculated parameters of ZnO based ceramics

#	Specimen	*a*/c (for ZnO) (nm)	*B* (for $Zn_x(Me)_yO_4$) (nm)	d_1 (kg/m^3)	d_2 (kg/m^3)	d_3 (kg/m^3)	d_0 (kg/m^3)	Π (%)
1	ZnO	0.324719 / 0.519646	–	5667	–	–	5036	11
2	$(ZnO)_{90}(CoO)_{10}$-2	0.324949 / 0.519748	0.807038 (or 0.86969 for Co_3O_4)	5658	3120	5633	4450	21
3	$(ZnO)_{97}(Al_2O_3)_3$	0.324770 / 0.519884	0.807548	5663	2307	5562	4200	24
4	$(ZnO)_{95}(Al_2O_3)_5$	0.324964 / 0.520207	0.808657	5653	2298	5485	3200	42
5	$(ZnO)_{97}(Al_2O_3)_3$	0.324563 / 0.519568	0.807476	5674	2308	5573	4780	14
6	$(ZnO)_{96.5}(Al_2O_3)_3(NiO)_{0.5}$	0.324813 / 0.519993	0.808001	5660	2303	5531	4260	23
7	$(ZnO)_{96.5}(Al_2O_3)_3(Fe_2O_3)_{0.5}$	0.325265 / 0.520535	0.810126	5639	2285	5510	4300	22
8	$(ZnO)_{96.5}(Al_2O_3)_3(Fe_3O_4–SiO_2)_{0.5}$	0.325199 / 0.520596	0.808865	5640	2296	5512	4100	26
9	$(ZnO)_{90}(TiO_2)_{10}$	0.325040 / 0.520823	0.846505	5643	2649	5344	5240	2

– for the total of the $ZnO + Zn_x(Me)_yO_4$ phases:

$$d_3 = \frac{100-z}{100}d_1 + \frac{z}{100}d_2 = \frac{100-z}{100}\frac{N_1A_1}{V_1} + \\ + \frac{z}{100}\frac{N_2A_2}{V_2} = \frac{100-z}{100}\frac{2N_1A_1}{3\sqrt{3}a^2c} + \frac{z}{100}\frac{N_2A_2}{b^3}. \quad (5)$$

Here

$$V_1 = \frac{6a^2\sqrt{3}}{4}C$$

is the hexagonal unit cell volume, $N_1 = 6$ is the number of atoms per hexagonal unit cell, $N_2 = 4$ is the number of atoms per cubic unit cell, A_i is the mass of one atom in a.m.u (1 a.m.u. = $1.66 \cdot 10^{-24}$ g), $A_1 = 81$ (for ZnO), $A_2 = 242$ for Zn_2TiO_4, 183 for $ZnAl_2O_4$ and 247 for $ZnCo_2O_4$; a and c are the ZnO lattice parameters (wurtzite), b is the $Zn_x(Me)_yO_z$lattice parameter (spinel), and z = 3–10 wt.% is the impurity weight percentage in ceramics except $(ZnO)_{90}(CoO)_{10}$-2 (Specimen 2) for which z was accepted as unity in Eq. (5) due to a high CoO solubility in wurtzite.

The X-ray densities d_1, d_2 and d_3 calculated using Eqs. (3)–(5) are summarized in Table 2. It can be seen from Table 2 that the X-ray density d_1 of the ZnO phase itself (i.e., without $Zn_x(Me)_yO_4$) in Specimens 2–9 depends but slightly on the type and quantity of doping impurity. However, the X-ray density of the final ceramic d_3 containing metal oxides (Specimens 2–9) decreases as compared with d_1. This can be accounted for by the fact that the overwhelming majority of Al_2O_3 and TiO_2 weight is spent for the formation of the $ZnAl_2O_4$ and Zn_2TiO_4 cubic spinels the X-ray density d_2 of which is lower than that of hexagonal ZnOd_1.

The difference between the X-ray densities d_1 (ZnO), d_3 ($ZnO + Zn_x(Me)_yO_4$) and d_0 of the final specimens (Table 2) as determined by weighing is caused by pores in the ceramics. This allowed calculating the porosity of the specimens using Eq. (6) for ZnO (Specimen 1) and Eq. (7) for Specimens 2–9:

$$\Pi = \left(1 - \frac{d_0}{d_1}\right)\cdot 100\%; \quad (6)$$

$$\Pi = \left(1 - \frac{d_0}{d_3}\right)\cdot 100\%; \quad (7)$$

As can be seen From Table 2, Me_xO_y oxide addition to ZnO powder increases the porosity of the ceramics by up to 42% which is probably caused by presence of the additional $Zn_x(Me)_yO_4$ spinel phase (Specimen 4), as well as by the differences between the raw powders and the annealing modes for undoped and doped zinc oxide.

SEM data are shown in Fig. 2. The doped $(ZnO)_{90}(CoO)_{10}$-2 two-stage annealed specimen exhibits a decline in grain size (Fig. 2 *b*) as compared with the undoped zinc oxide specimen (Fig. 2 *a*). We showed earlier that grain sizes in one-stage annealed ceramics with iron oxide additions were also greater than those in similar powders after two-stage annealing [20, 21]. We therefore attribute the smaller grain size in the two-stage annealed ceramics to an increase in the number of recrystallization centers at granule boundaries of tablet specimens as a result of the second grinding. It also follows from Fig. 2 that less dense specimens have larger grains.

4. Thermal properties of composite ceramics

The thermo-emf coefficient S and the electrical resistivity ρ of the test specimens were measured at room tempera-

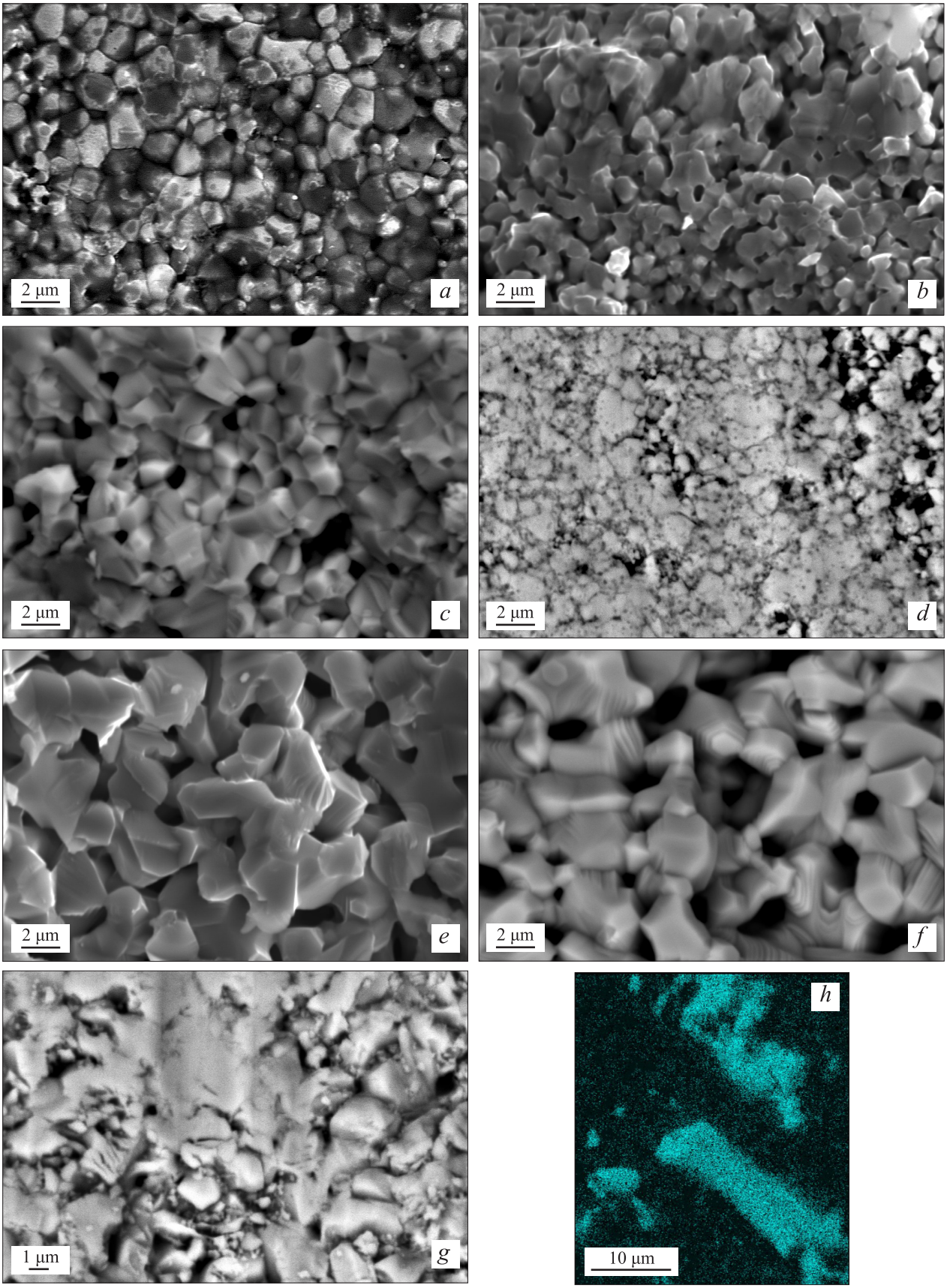

Figure 2. SEM images of ceramics: (*a*) ZnO, (*b*) $(ZnO)_{90}(CoO)_{10}$-2, (*c*) $(ZnO)_{90}(TiO_2)_{10}$, (*d*) $(ZnO)_{97}(Al_2O_3)_3$ (Specimen 5), (*e*) $(ZnO)_{96.5}(Al_2O_3)_3(Fe_2O_3)_{0.5}$, (*f*) $(ZnO)_{96.5}(Al_2O_3)_3(Fe_3O_4\text{-}SiO_2)_{0.5}$, (*g*) $(ZnO)_{95}(Al_2O_3)_5$ and (*h*) EDX aluminum distribution for $(ZnO)_{96.5}(Al_2O_3)_3(NiO)_{0.5}$

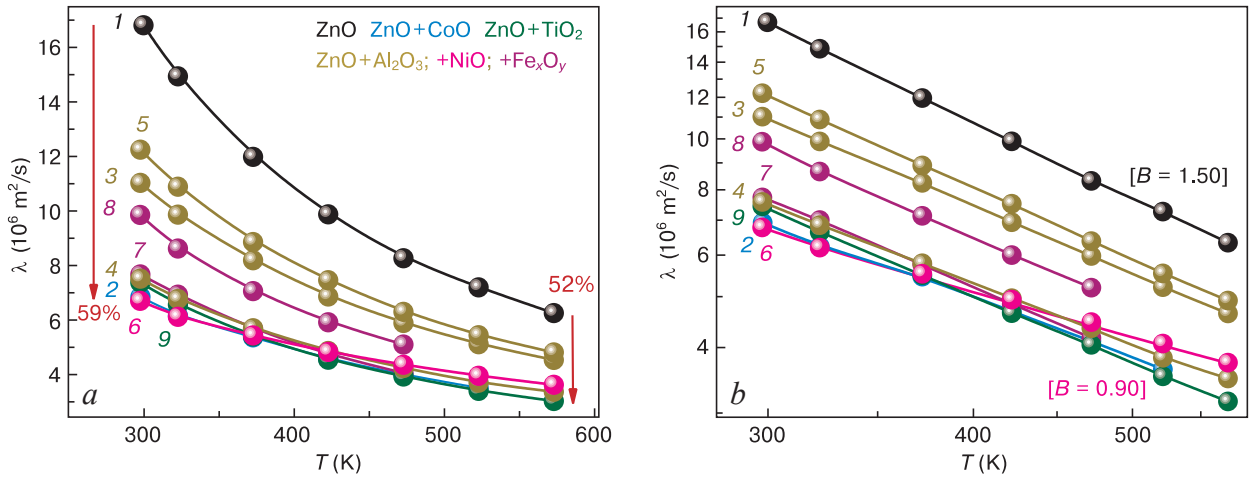

Figure 3. Temperature conductivity λ of test ceramics as a function of temperature in (*a*) linear and (*b*) double logarithmic scales: (*1*) ZnO; (*2*) $(ZnO)_{90}(CoO)_{10}$-2; (*3*) $(ZnO)_{97}(Al_2O_3)_3$; (*4*) $(ZnO)_{95}(Al_2O_3)_5$; (*5*) $(ZnO)_{97}(Al_2O_3)_3$; (*6*) $(ZnO)_{96.5}(Al_2O_3)_3(NiO)_{0.5}$; (*7*) $(ZnO)_{96.5}(Al_2O_3)_3(Fe_2O_3)_{0.5}$; (*8*) $ZnO)_{96.5}(Al_2O_3)_3(Fe_3O_4\text{-}SiO_2)_{0.5}$; (*9*) $(ZnO)_{90}(TiO_2)_{10}$

ture (300 K), and the temperature conductivity λ(*T*) was measured at 300–600 K. The λ(*T*) curves are shown in Fig. 3 *a*. These curves can be described by a hyperbolic law such as

$$\lambda(T) \sim T^{-B}, \quad (8)$$

where the exponent B, according to Table 3, is in the $B \approx 0.90$–1.50 range. The *B* parameter was determined from the slope of the lg λ *vs* lg *T* lines in Fig. 3 *b*. As can be seen from Fig. 3 *a*, the temperature conductivity at 300 K decreased as a result of ceramic doping somewhat greater than at high temperatures. This can be accounted for by a decrease in the lattice contribution to the temperature conductivity with an increase in temperature [14, 18, 22, 28, 29].

Equation (2) suggests that to determine the temperature dependence of the temperature conductivity κ(*T*) of the specimens it is required to know their heat capacity C_p and density d_0. The temperature dependence of the isobaric specific heat $C_p(T)$ in the 300–600 K range for the test specimens was evaluated using the Neuman–Kopp method [30]. $C_p(T)$ functions for different phases burrowed from literature [31] are shown in Fig. 4 *a*. For this method the specific heat of doped ceramics is approximated as the sum of the specific heat of the constituent phases taking into account their weight fractions in the $(ZnO)_{100-z}(Me_xO_y)_z$ ceramic where $z = 3 \div 10$ is the weight fraction of metal oxide powders in the test specimens in wt.%. As can be seen from Fig. 4 *a*, the isobaric specific heat C_p of the phases and the ceramics varies in accordance with the following law:

$$C_p(T) \sim T^A, \quad (9)$$

where $A \approx 0.20$–0.25. It was accepted for the calculations that almost all the added metal oxide is spent for the formation of the $Zn_x(Me)_yO_4$ spinel the fraction of

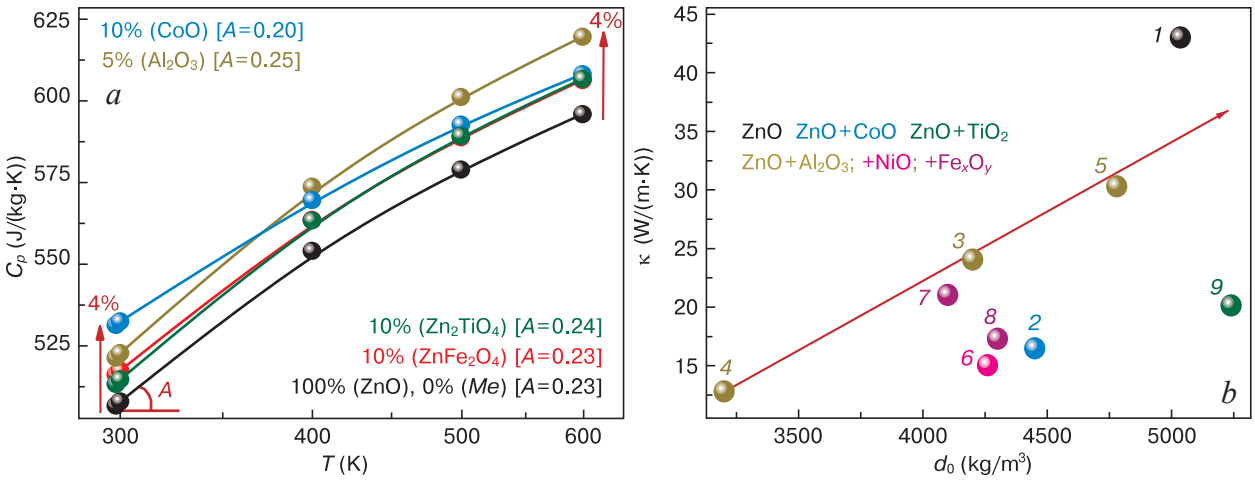

Figure 4. (*a*) Temperature dependences of isobaric specific heat C_p of total materials in percents [31] and (*b*) heat conductivity κ as a function of density d_0 for test ceramics at $T = 300$ K in a linear scale. *b*: (*1*) ZnO; (*2*) $(ZnO)_{90}(CoO)_{10}$-2; (*3*) $(ZnO)_{97}(Al_2O_3)_3$; (*4*) $(ZnO)_{95}(Al_2O_3)_5$; (*5*) $(ZnO)_{97}(Al_2O_3)_3$; (*6*) $(ZnO)_{96.5}(Al_2O_3)_3(NiO)_{0.5}$; (*7*) $(ZnO)_{96.5}(Al_2O_3)_3(Fe_2O_3)_{0.5}$; (*8*) $ZnO)_{96.5}(Al_2O_3)_3(Fe_3O_4\text{-}SiO_2)_{0.5}$; (*9*) $(ZnO)_{90}(TiO_2)_{10}$

which cannot exceed 10% of the total weight of ceramics. The presence of $Zn_x(Me)_yO_4$ increases the specific heat by not more than 4% (see Fig. 4 *a*) and only slightly affects the behavior of the temperature conductivity upon doping. The positions of the points in Fig. 4 *b* suggest a nearly linear pattern of the heat conductivity as a function of density except for the titanium doped specimen $(ZnO)_{90}(TiO_2)_{10}$ having one of the lowest temperature conductivities.

The experimental densities d_0 (see Fig. 4 *b*) and the $\lambda(T)$ curves of the studied specimens, as well as their isobaric specific heat C_p (see Fig. 4 *a*) allow evaluating the temperature dependences of the heat conductivity $\kappa(T)$ for the specimens using Eq. (2). As can be seen from Fig. 5 *a*, the $\kappa(T)$ function can be described as

$$\kappa(T) \sim T^{-C}, \tag{10}$$

where the C values as determined from the slopes of the $\lg\kappa$ *vs* $\lg T$ lines in Fig. 5 *b* are summarized in Table 3.

Potential electron contribution κ_e to the full heat conductivity was determined using the Wiedemann–Franz method [29, 32]:

$$\kappa_e = \frac{LT}{\rho}, \tag{11}$$

in which the Lorenz number was calculated through the thermo-emf coefficient S using the formula

$$L = \left(1.5 + \exp\left[-\frac{|S|}{116}\right]\right)\cdot 10^{-8}, \tag{12}$$

obtained by solving Boltzmann transfer equations [32]. The components' contributions to the full heat conductivity summarized in Table 3 suggest that the lattice component has the predominant contribution to Eq. (2), i.e., $\kappa \approx \kappa_l$, since the electron contribution κ_e evaluated using Eqs. (11) and (12) is incomparably small. Therefore the decline of the ionic conductivity with an increase in temperature and the difference in the behavior of the $\kappa(T)$

Table 3. Experimental temperature conductivity λ, exponents in Eqs. (8)–(10), electron κ_e and lattice $\kappa_l \approx \kappa$ contributions to heat conductivity κ for ceramic specimens at 300 K

#	Speimen	λ (10^{-6} m²/s)	*A*	*B*	*C*	κ_e (W/(m·K))	κ_l (W/(m·K))
1	ZnO	16.8	0.23	1.50	1.27	$1.19\cdot10^{-7}$	43.05
2	$(ZnO)_{90}(CoO)_{10}$-2	6.94	0.20 (0.23)	1.14	0.93	$2.21\cdot10^{-7}$	16.36
3	$(ZnO)_{97}(Al_2O_3)_3$	11.1	0.25	1.33	1.09	$2.59\cdot10^{-5}$	23.98
4	$(ZnO)_{95}(Al_2O_3)_5$	7.60	0.26	1.20	0.96	$1.46\cdot10^{-4}$	12.66
5	$(ZnO)_{97}(Al_2O_3)_3$	12.3	0.25	1.41	1.16	$4.59\cdot10^{-5}$	30.27
6	$(ZnO)_{97}(Al_2O_3)_3(NiO)_{0.5}$	6.79	0.25	0.90	0.65	$1.56\cdot10^{-3}$	14.91
7	$(ZnO)_{97}(Al_2O_3)_3(Fe_2O_3)_{0.5}$	7.76	0.25	1.35	1.08	$8.56\cdot10^{-7}$	17.18
8	$(ZnO)_{97}(Al_2O_3)_3(Fe_3O_4\text{-}SiO_2)_{0.5}$	9.92	0.25	1.39	1.11	$1.16\cdot10^{-6}$	20.95
9	$(ZnO)_{90}(TiO_2)_{10}$	7.46	0.24	1.32	1.08	$2.31\cdot10^{-4}$	20.05

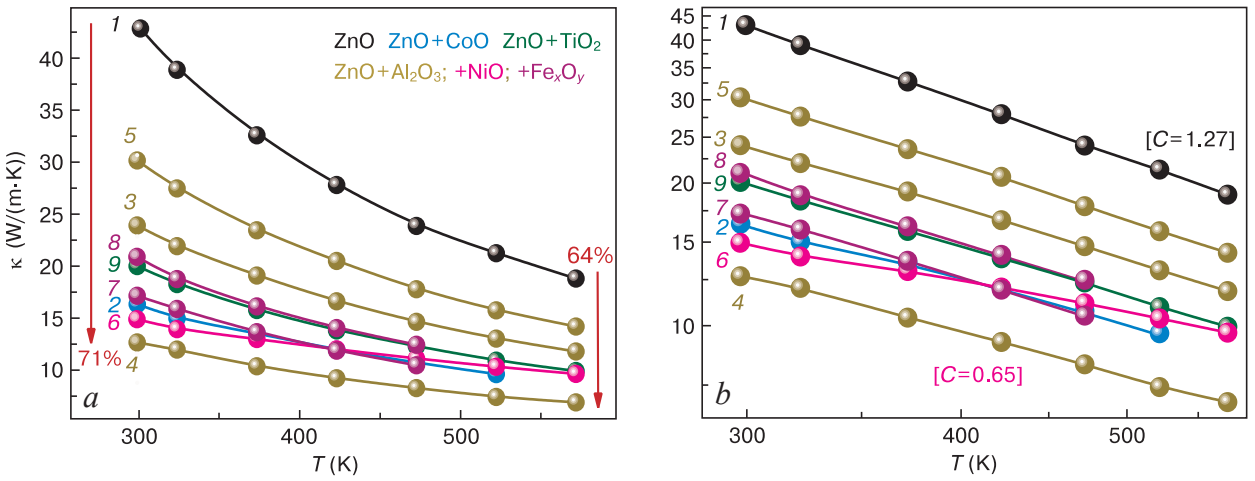

Figure 5. Heat conductivity κ of test ceramics as a function of temperature in (*a*) linear and (*b*) double logarithmic scales: (*1*) ZnO; (*2*) $(ZnO)_{90}(CoO)_{10}$-2; (*3*) $(ZnO)_{97}(Al_2O_3)_3$; (*4*) $(ZnO)_{95}(Al_2O_3)_5$; (*5*) $(ZnO)_{97}(Al_2O_3)_3$; (*6*) $(ZnO)_{96.5}(Al_2O_3)_3(NiO)_{0.5}$; (*7*) $(ZnO)_{96.5}(Al_2O_3)_3(Fe_2O_3)_{0.5}$; (*8*) $(ZnO)_{96.5}(Al_2O_3)_3(Fe_3O_4\text{-}SiO_2)_{0.5}$; (*9*) $(ZnO)_{90}(TiO_2)_{10}$

Table 4. Thermoelectric, electrical and thermal parameters of ZnO based ceramics at 300 K

#	Specimen	ρ (Ohm · m)	–*S* (mV/K)	*P* (W/(m · K²))	κ_e (W/(m · K))	*ZT*
1	ZnO	$3.67 \cdot 10^{1}$	385	$4.04 \cdot 10^{-9}$	43.05	$2.81 \cdot 10^{-8}$
	ZnO (ann)*	$3.80 \cdot 10^{1}$	435	$4.99 \cdot 10^{-9}$		$3.47 \cdot 10^{-8}$
2	$(ZnO)_{90}(CoO)_{10}$-2	$5.10 \cdot 10^{0}$	580	$1.65 \cdot 10^{-8}$	16.36	$3.02 \cdot 10^{-7}$
3	$(ZnO)_{97}(Al_2O_3)_3$	$1.90 \cdot 10^{-1}$	221	$2.57 \cdot 10^{-7}$	23.98	$3.20 \cdot 10^{-6}$
4	$(ZnO)_{95}(Al_2O_3)_5$	$3.19 \cdot 10^{-2}$	346	$3.75 \cdot 10^{-6}$	12.66	$8.88 \cdot 10^{-5}$
5	$(ZnO)_{97}(Al_2O_3)_3$	$1.07 \cdot 10^{-1}$	229	$4.90 \cdot 10^{-7}$	30.27	$4.86 \cdot 10^{-6}$
6	$(ZnO)_{97}(Al_2O_3)_3(NiO)_{0.5}$	$2.46 \cdot 10^{0}$	224	$2.04 \cdot 10^{-8}$	14.91	$4.10 \cdot 10^{-7}$
	$(ZnO)_{97}(Al_2O_3)_3(NiO)_{0.5}$ (ann)	$3.06 \cdot 10^{-3}$	278	$2.53 \cdot 10^{-5}$		$5.08 \cdot 10^{-4}$
7	$(ZnO)_{97}(Al_2O_3)_3(Fe_2O_3)_{0.5}$	$5.46 \cdot 10^{0}$	330	$2.00 \cdot 10^{-8}$	17.18	$3.48 \cdot 10^{-7}$
8	$(ZnO)_{97}(Al_2O_3)_3(Fe_3O_4–SiO_2)_{0.5}$	$4.14 \cdot 10^{0}$	276	$1.84 \cdot 10^{-8}$	20.95	$2.64 \cdot 10^{-7}$
9	$(ZnO)_{90}(TiO_2)_{10}$	$2.30 \cdot 10^{-2}$	162	$1.14 \cdot 10^{-6}$	20.05	$1.46 \cdot 10^{-5}$

*The notation "ann" marks specimens for which properties were measured after high-temperature measurements.

curves at high and low temperatures should only be accounted for by the contribution of the phonon spectrum.

Comparison of the temperature dependences of the phonon heat conductivity (Eq. (10)) and the temperature conductivity (Eq. (8)) shown in Figs. 5 *a* and 3 *a* suggests that the difference in their exponents $B - C = A$ exactly equals the exponent of the temperature dependence of the isobaric heat capacity (Eq. (9). The behavior of the temperature dependence of the heat conductivity is in agreement with well-known literary data [4, 29, 33]: the decline of $\kappa(T)$ is attributed to the growth of phonon-phonon scattering with an increase in temperature. It should be noted that the heat conductivity and the temperature conductivity behave quite similarly.

The difference between the heat conductivity of raw zinc oxide and those of doped ceramics (as well as many other semiconductors) is typically associated with the wide gap between the optical and the acoustic branches in the phonon dispersion law. The latter fact may significantly distort the energy and quasi-impulse conservation laws for three-phonon scattering and increase the phonon lifetime, which can be potentially coupled with anharmonicity (the Gruneisen parameter) and large phonon group velocities (due to stronger interatomic bonds) [4].

By and large, the decline in the heat conductivity seen from Fig. 5 *a* upon metal oxide addition to ZnO based ceramics can be accounted for by the following four factors:

– greater phonon scattering at point defects formed due to zinc ion substitution for metal ions in the ZnO lattice;

– stronger phonon scattering at grain boundaries due to microstructure refinement (greater total grain boundary area) [14];

– growth of the porosity of ceramics as a result of doping [33];

– precipitation of the $Zn_x(Me)_yO_4$ phase with a layered spinel-like structure causing additional phonon scattering.

5. Thermoelectric efficiency of composite ceramics

The power factor *PF* [29]

$$PF = \frac{S^2}{\rho}$$

and the dimensionless figure-of-art *ZT* in Eq. (1) [32] were calculated on the basis of experimentally measured *S* and ρ at 300 K which are summarized in Table 4.

It follows from Table 4 that addition of metals to ZnO ceramics increases the figure-of-art (by almost four orders of magnitude for Specimen 6) in comparison with that for undoped ZnO ceramics [8, 9] (see also [14]). This is caused by the decrease in the electrical resistivity by four orders of magnitude (which can be attributed to extrinsic conductivity caused by the formation of small donor centers having a low ionization energy [20]), as well as by the decline in the heat conductivity as described herein. Noteworthy, the greatest augment of the figure-of-art is observed for the specimen doped with Al and Ni (Specimen 6) and subjected to high-temperature measurements that are in fact an additional anneal. The figure-of-art of ZnO ceramics differs from that of the same ceramic composition without additional annealing (Specimen 6) by only three orders of magnitude due to a lower electrical resistivity (Table 4). For undoped zinc oxide ceramic (Specimen 1), additional annealing did not increase the figure-of-art by orders of magnitude. This is because additional annealing leads to a more

homogeneous distribution of doping metal ions in the wurtzite lattice thus entailing an increase in the number of donor centers that are favorable for electrical conductivity [20].

6. Conclusion

The thermal, electrical and thermoelectric properties of ceramics ZnO–Me_xO_y with $1 \le x, y \le 3$, where *Me* = Al, Co, Fe, Ni, Ti, were studied. X-ray diffraction data suggest that addition of Me_xO_y doping powders to ZnO powder with a wurtzite structure causes spinel-like $Zn_x(Me)_yO_4$ secondary phase precipitations and a four-fold growth of the porosity after synthesis. Lattice heat conductivity is predominant in the ceramics at room temperature but its contribution decreases with an increase in temperature. The decline in the heat conductivity upon doping is favored by an increase in phonon scattering at grain boundaries, at point defects forming due to zinc ion substitution for doping metal ions, at pores and at additional $Zn_x(Me)_yO_4$ phase precipitates. In the Al, Co, Fe, Ni and Ti doped ceramics, the decline in the heat conductivity and the decrease in the electrical resistivity by orders of magnitude combined with a moderate change of the termo-emf coefficient provide for a growth of the figure-of-art by four orders of magnitude. Longer annealing reduces the electrical resistivity due to a more homogeneous distribution of doping metal ions in the wurtzite lattice which is favorable for the growth of donor centers.

Acknowledgement

This research was funded by the State program of scientific research “PhysMatTech, New Materials and Technologies” (Belarus) under grant number 1.15.1.

References

1. Ponja S.D., Sathasivam S., Parkin I.P., Carmalt C.J. Highly conductive and transparent gallium doped zinc oxide thin films via chemical vapor deposition. *Scientific Reports.* 2020; 10(1): 638. https://doi.org/10.1038/s41598-020-57532-7
2. Lee Y.-P., Lin Ch-Ch., Hsiao Ch-Ch., Chou P.-A., Cheng Y.-Y., Hsieh Ch-Ch., Dai Ch-A. Nanopiezoelectric devices for energy generation based on ZnO nanorods / flexible-conjugated copolymer hybrids using all wet-coating processes. *Micromachines.* 2020; 11(1): 14. https://doi.org/10.3390/mi11010014
3. Bernik S., Daneu N. Characteristics of SnO_2-doped ZnO-based varistor ceramics. *Journal of the European Ceramic Society.* 2001; 21(10-11): 1879–1882. https://doi.org/10.1016/S0955-2219(01)00135-2
4. Wu X., Lee J., Varshney V., Wohlwend J.L., Roy A.K., Luo T. Thermal conductivity of wurtzite zinc-oxide from first-principles lattice dynamics – a comparative study with gallium nitride. *Scientific Reports*. 2016; 6(1): 22504. https://doi.org/10.1038/srep22504
5. Sawalha A., Abu-Abdeen M., Sedky A. Electrical conductivity study in pure and doped ZnO ceramic system. *Physica B: Condensed Matter.* 2009; 404(8-11): 1316–1320. https://doi.org/10.1016/j.physb.2008.12.017
6. Winarski D. Synthesis and characterization of transparent conductive zinc oxide thin films by sol-gel spin coating method. Thesis diss. of master science. Graduate College of Bowling Green State University; 2015.
7. Chen H., Zheng L., Zeng J., Li G., Effect of Sr doping on nonlinear current-voltage properties of ZnO-based ceramics. *Journal of Electronic Materials*. 2021; 50(7): 4096–4103. https://doi.org/ 10.1007/s11664-021-08960-2
8. Mohammed M.A., Izman S., Alias M.N., Rajoo S., Uday M.B., Obayes N.H., Omar M.F. A review of thermoelectric ZnO nanostructured ceramics for energy recovery. International *Journal of Engineering & Technology.* 2018; 7(2.29): 27–30. https://doi.org/10.14419/IJET.V7I2.29.13120
9. Colder H., Guilmeau E., Harnois C., Marinel S., Retoux R., Savary E. Preparation of Ni-doped ZnO ceramics for thermoelectric applications. *Journal of the European Ceramic Society*. 2011; 31(15): 2957–2963. https://doi.org/10.1016/j.jeurceramsoc.2011.07.006
10. Jeong A., Suekuni K., Ohtakia M., Jang B.-K. Thermoelectric properties of In- and Ga-doped spark plasma sintered ZnO ceramics. *Ceramics International.* 2021; 47(17): 23927–23934. https://doi.org/10.1016/j.ceramint.2021.05.101
11. Levinson L.M., Hirano S. Ceramic transactions. In: *Procced. of Inter. symposium. Vol. 41. Grain boundaries and interfacial phenomena in electronic ceramics*. Westerville: American Ceramic Society; 1994.
12. Li J., Yang S., Pu Y., Zhu D. Effects of pre-calcination and sintering temperature on the microstructure and electrical properties of ZnO-based varistor ceramics. *Materials Science in Semiconductor Processing.* 2021; 123(6): 105529. https://doi.org/10.1016/j.mssp.2020.105529
13. Liang X. Thermoelectric transport properties of naturally nanostructured Ga–ZnO ceramics: Effect of point defect and interfaces. *Journal of the European Ceramic Society.* 2016; 36(7): 1643–1650. https://doi.org/10.1016/j.jeurceramsoc.2016.02.017
14. Liang X. Thermoelectric transport properties of Fe-enriched ZnO with high- temperature nanostructure refinement. *ACS Applied Materials & Interfaces.* 2015; 7(15): 7927–7937. https://doi.org/10.1021/am509050a
15. Walia S., Balendhran S., Nili H., Zhuiykov S., Rosengarten G., Wang Q.H., Bhaskaran M., Sriram S., Strano M.S., Kalantar-zadeh K. Transition metal oxides – thermoelectric properties. *Progress in Materials Science.* 2013; 58(8): 1443–1489. https://doi.org/10.1016/j.pmatsci.2013.06.003
16. Li P., Zhang H., Gao C., Jiang G., Li Z. Electrical property of Al/La/Cu modified ZnO-based negative temperature coefficient (NTC) ceramics with high ageing stability. *Journal of Materials Science:*

Materials in Electronics. 2019; 30(21): 19598–19608. https://doi.org/10.1007/s10854-019-02333-6

17. Pullar R.C., Piccirilloa C., Novais R.M., Quarta A., Bettini S., Iafisco M. A sustainable multi-function biomorphic material for pollution remediation or UV absorption: aerosol assisted preparation of highly porous ZnO-based materials from cork templates. *Journal of Environmental Chemical Engineering.* 2019; 7(2): 102936. https://doi.org/10.1016/j.jece.2019.102936
18. Sun Q., Li G., Tian T., Zeng J., Zhao K., Zheng L., Barre M., Dittmer J., Gouttenoire F., Rousseau A., Kassiba A.H. Co-doping effects of (Al, Ti, Mg) on the microstructure and electrical behavior of ZnO-based ceramics. *Journal of the American Ceramic Society*. 2020; 103(5): 3194–3204. https://doi.org/10.1111/jace.16999
19. Vu D.V., Le D.H., Nguyen C.X., Trinh T.Q. Comparison of structural and electric properties of ZnO-based *n*-type thin films with different dopants for thermoelectric applications. *Journal of Sol-Gel Science and Technology.* 2019; 91(1): 146–153. https://doi.org/10.1007/s10971-019-05024-0
20. Pashkevich A.V., Fedotov A.K., Poddenezhny E.N., Bliznyuk L.A., Fedotova J.A., Basov N.A., Kharchanka A.A., Zukowski P., Koltunowicz T.N., Korolik O.V., Fedotova V.V. Structure, electric and thermoelectric properties of binary ZnO-based ceramics doped with Fe and Co. *Journal of Alloys and Compounds.* 2022; 895: 162621. https://doi.org/10.1016/j.jallcom.2021.162621
21. Pashkevich A.V., Bliznyuk L.A., Fedotov A.K., Khovaylo V.V., Fedotova V.V., Kharchanka A.A. Thermal and thermoelectric properties of ceramics based on zinc oxide alloyed with iron. *Zhurnal Belorusskogo gosudarstvennogo universiteta. Fizika.* 2022; (3): 56–67. (In Russ.). https://doi.org/10.33581/2520-2243-2022-3-56-67
22. Wu Z.-H., Xie H.-Q., Zhai Y.-B. Preparation and thermoelectric properties of Co-doped ZnO synthesized by sol-gel. *Journal of Nanoscience and Nanotechnology.* 2015; 15(4): 3147–3150. https://doi.org/10.1166/jnn.2015.9658
23. Sawalha A., Abu-Abdeen M., Sedky A. Electrical conductivity study in pure and doped ZnO ceramic system. *Physica B Condensed Matter.* 2009; 404(8-11): 1316–1320. https://doi.org/10.1016/j.physb.2008.12.017
24. Gorokhova E.I., Anan'eva G.V., Eron'ko S.B., Oreshchenko E.A., Rodnyi P.A., Chernenko K.A., Khodyuk I.V., Lokshin E.P., Kunshina G.B., Gromov O.G., Lott K.P. Structural, optical, and scintillation characteristics of ZnO ceramics. *Journal of Optical Technology*.2011; 78(11): 733–760. https://doi.org/10.1364/jot.78.000753
25. Krzhizhanovskaya M.G., Firsova V.A., Bubnova R.S. Application of the Rietveld method for solving problems of powder diffractometry. St. Petersburg: Sankt-Peterburgskii universitet; 2016. 67 p. (In Russ.)
26. Zeer G.M., Fomenko O.Yu., Ledyaeva O.N. Application of scanning electron microscopy in material science. *Zhurnal Sibirskogo federal'nogo universiteta. Seriya: Khimiya = Journal of Siberian Federal University. Chemistry.* 2009; 4(2): 287–293. (In Russ.)
27. Bosi F., Biagioni C., Pasero M. Nomenclature and classification of the spinel supergroup. *European Journal of Mineralogy.* 2019; 31(1): 183–192. https://doi.org/10.1127/ejm/2019/0031-2788
28. Cheng H., Xu X.J., Hng H.H., Ma J. Characterization of Al-doped ZnO thermoelectric materials prepared by RF plasma powder processing and hot press sintering. *Ceramics International.* 2009; 35(8): 3067–3072. https://doi.org/10.1016/j.ceramint.2009.04.010
29. Chernyshova E., Serhiienko I., Kolesnikov E., Voronin A., Zheleznyy M., Fedotov A., Khovaylo V. Influence of NiO nanoparticles on the thermoelectric propertiesof $(ZnO)_{1-x}(NiO)_x$ composites. *Nanobiotechnology Reports.* 2021; 16(3): 381–386. https://doi.org/10.1134/S2635167621030034
30. Adun H., Kavaz D., Wole-Osho I., Dagbasi M. Synthesis of Fe_3O_4–Al_2O_3–ZnO / water ternary hybrid nanofluid: Investigating the effects of temperature, volume concentration and mixture ratio on specific heat capacity, and development of hybrid machine learning for prediction. *Journal of Energy Storage.* 2021; 41(13-14): 102947. https://doi.org/10.1016/j.est.2021.102947
31. Barin I. Thermochemical data of pure substances. Weinheim, Federal Republic of Germany; N.Y., USA: VCH; 1995. 2003 p.
32. Kim H.-S., Gibbs Z.M., Tang Y., Wang H., Snyder G.J. Characterization of Lorenz number with Seebeck coefficient measurement. *APL Materials.* 2015; 3(4): 041506. https://doi.org/10.1063/1.4908244
33. Gadzhiev G.G. The thermal and elastic properties of zinc oxide-based ceramics at high temperatures. *High Temperature.* 2003; 41(6): 778–782. https://doi.org/10.1023/b:hite.0000008333.59304.58